ELSEVIER

Statistical analysis of fractal-based brain tumor detection algorithms

Justin M. Zook[a], Khan M. Iftekharuddin[b],*

[a]*Department of Biomedical Engineering, The University of Memphis, TN 38152-3810, USA*
[b]*Department of Electrical and Computer Engineering, The University of Memphis, TN 38152-3810, USA*

Abstract

Fractals are geometric objects that have a noninteger fractal dimension (FD). The FD has been exploited for various biomedical recognition applications such as breast tumor and lung tumor detection. Our previous work shows that the FD is useful in the detection of brain tumors when a reference nontumor image is available. In this work, we extend our previous work by statistically validating the results of FD analysis on a set of 80 real MR and CT images. Our half-image technique requires that the tumor is located in one half of the brain whereas our whole-image technique does not. Furthermore, we alleviate the need for a reference (control) nontumor image to compute the tumor FD, which was necessary in our previous work. We also compare the brain tumor detection performance of our algorithms with other fractal-based algorithms in the literature and statistically validate our results against manually segmented tumor images. We find that the tumor region offers a statistically significant lower FD compared with that of the nontumor area for most of the FD algorithms studied in this work. Thus, our statistical analysis suggests that these FD algorithms may be exploited successfully to determine the possible presence and location of brain tumors in MR and CT images.
© 2005 Elsevier Inc. All rights reserved.

Keywords: Fractal dimension analysis; Tumor detection; MR images; CT images; Statistical analysis

1. Introduction

Brain tumors are an attractive candidate for computer-assisted detection. In a typical clinic, radiologists review a large number of MR and CT images per day for tumor detection. This process is very tedious and prone to error when the radiologists have a limited amount of time. The problem is compounded further when tumors are small. In addition, an automated tumor segmentation procedure is needed for image-guided surgery. Thus, automated tumor segmentation tools may aid medical practitioners and users manifold.

Although many algorithms have been proposed in the literature for brain tissue segmentation, most of them are ineffective for tumor tissue segmentation [1]. Large tumors have generally been segmented with manual tracing or with semiautomated low-level computer vision tools. Fully automated methods can be classified into two general groups: a region-based group and a contour-based group. Region-based techniques attempt to differentiate tumor regions from nontumor regions usually by low-level operations such as thresholding [2], edge detection and morphological operators [3,4]. One disadvantage of the region-based methods is that they require specific assumptions that are both application dependent (anatomy) and scan dependent (voxel size) to be made. Other research work have used neural networks [5,6] or statistical classification methods [7–9] that work variably well. However, these methods often fail to differentiate between active tumors, related pathologies and normal tissues. In contrast, contour-based methods locate the boundary of a tumor by using internal forces (e.g., curvature) and external forces (e.g., image gradients). These methods have drawbacks similar to those of the region-based methods, such that the tumor area needs to be easily separable from the surrounding tissue [5,10,11].

In a previous work, we proposed fractal dimension (FD) analysis techniques to alleviate some of these problems in the analysis of brain tumor images [12]. Fractals are found in many places in nature, including ferns, mountains, bacteria, snowflakes, clouds and coastlines. While Euclidean geometrical objects always have integer topological dimensions, fractal objects, by definition, have a noninteger FD. In the

---

* Corresponding author. Tel.: +1 901 678 3250; fax: +1 901 678 5469.
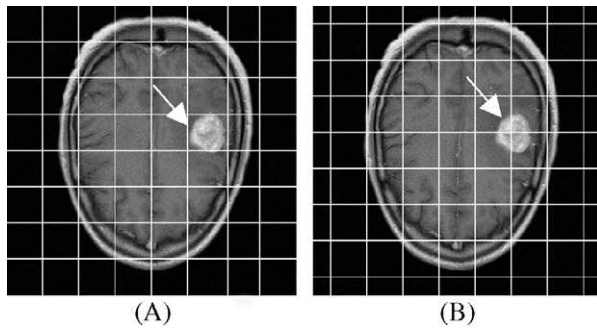*E-mail address:* iftekhar@memphis.edu (K.M. Iftekharuddin).

Fig. 1. (A) Nontranslated subimages. (B) Translated subimages.

past, the FD has been exploited to measure surface roughness [13,14], microcalcifications in mammograms [15,16] and small lung tumors [17]. Some parts of the human body, such as the lungs and trabecular bone, also appear to grow in the form of fractals. Thus, it is reasonable to predict that other elements of the body, such as brain tissues or tumors, may also exhibit fractal characteristics. Consequently, we have exploited FD analysis to detect brain tumors [12].

The purpose of this research was to extend our previous work [12] by investigating the results of FD analysis on a set of MR and CT images for statistical validation. In the previous work, we used the FD to locate the tumor region by comparing a brain MR image with an identical reference image without the tumor [12]. However, in most cases, a nontumor reference image may not be available for patients. Thus, in this work, we eliminated the need for a reference image by comparing the FD of the left half of the brain with that of the right half, assuming that the tumor is located in only one half. We also compared the average FD of tumor regions with that of nontumor regions. Finally, the average FD of each half of the brain was computed to locate the tumor in one half of the image.

The efficacy of the FD analysis method for detecting brain tumors was evaluated in MR and CT images. The MR image set included four modalities, including proton density, T1, T2 and fluid attenuation inversion recovery (FLAIR) images with and without a contrast agent. We investigated the performance of the piecewise modified box counting (PMBC) and piecewise triangular prism surface area (PTPSA) algorithms [12], which are two of our previously reported algorithms for determining the FD. We compared

the tumor detection performance of our algorithms with that of the blanket algorithm, which is another fractal algorithm reported in the literature [15]. These algorithms were performed on images at four resolutions, with 8×8, 16×16, 32×32 or 64×64 subimages. Next, the tumor regions were manually segmented to obtain a reference benchmark for comparison. The reference benchmarks allowed us to determine the statistical significance of the difference between tumor and nontumor regions for the various imaging modalities. Consequently, these results may be used to determine how best one may exploit fractal analysis to obtain the location of a tumor in a given brain MR or CT image.

2. FD algorithms

In this section, we briefly review three relevant FD computation algorithms. Specifically, we used the PMBC, PTPSA and blanket algorithms. First, we divided each 256×256-pixel image into 8×8, 16×16, 32×32 and 64×64 subimages. An example of an MR image divided into 8×8 subimages is shown in Fig. 1(A). To determine whether our fractal algorithm computes a consistent FD even if the subimages are divided in a different manner, the subimages were translated by half of their width in each direction, as shown in Fig. 1(B). A comparison of the tumor area in Fig. 1(A) and (B) suggests that image translation may affect the number of subimages containing the tumor, which, in turn, may influence the detection of the tumor.

After dividing the image into subimages, we used one of the three algorithms to compute the FD for each subimage. The detailed algorithm for our PMBC technique is shown in Fig. 2. Each subimage was divided into boxes of several sizes, and the difference between the maximum and minimum gray values was computed for each box. The detailed algorithm for our PTPSA technique is shown in Fig. 3. Note that as in PMBC, we again divided each subimage into boxes of several sizes for the PTPSA algorithm. However, in PTPSA, a more accurate procedure using the four corner and center gray values was used. Finally, the PMBC and PTPSA algorithms were compared with the blanket algorithm. The detailed algorithm for the blanket method is shown in Fig. 4. For the blanket algorithm, each subimage was not divided into boxes. Instead, an

---

Algorithm 1

---

for *each sub-image*
    Divide sub-image into boxes of size n x n
    for *each box of size n x n*
        Find difference between max and min gray boxes
    Sum differences for entire sub-image
    FD = log(sum of differences)/log(n)

Fig. 2. Pseudocode for the PMBC algorithm [12,13].

Algorithm 2

---

for *each sub-image*

    Divide sub-image into boxes of size n x n

    for *each box of size n x n*

        Find the surface area of the four triangles formed by treating gray value as the third

        dimension and connecting the four corner points with the center point and each other.

    Sum surface areas for entire sub-image

    FD = log(sum of surface areas)/log(n)

Fig. 3. Pseudocode for the PTPSA algorithm [12,14].

iterative process in which each pixel was compared with its surrounding pixels was used.

3. Image data set and methods

We evaluated each of the FD algorithms using real MR and CT brain images. The algorithms were tested on two sets of brain images that contained tumors. Specifically, we tested (a) a set of 35 images from an American College of Radiology (ACR) CDROM and (b) a set of 45 images from the St. Jude Children's Research Hospital (SJ). The ACR images were both MR and CT images from a variety of patients. The SJ images were only MR images taken from several transverse slices from four patients. The specific number of images for each imaging modality in each data set is shown in Table 1. Note that all of our test images contained the tumor in only one half of the brain image. Furthermore, in this work, we refer "left" of the image to indicate the left part of an image from an observer's perspective, which is actually the right side of a patient's image in standard radiological convention. In addition, a tumor is shown using an arrow in all image examples.

Of the 35 ACR images, 23 were MR images and 12 were CT images. None of the MR and CT images were from the same patient. The specific patient and imaging details for the ACR images were not available for many images on the CD. However, all ACR images were transverse slices containing a tumor region and the images were resized to

256×256 pixels, if necessary. The 45 MR images from SJ have the following characteristics: the images were from a child/young adult data set and were performed on 1.5-T Siemens Magnetom scanners from Siemens Medical Systems. All images were in the transverse orientation with the following parameters: an average of 20 slices/patient, slice thickness of 5 mm, slice gap of 1 mm, field of view of 210×210 mm^2 and image matrix of 256×256 pixels. Pulse sequences included the following: T1-weighted (TR=165 ms, TE=6 ms, flip angle=60°), T2-weighted (Turbo Spin Echo, TR=6630, TE=115 ms, 15 echoes/TR), FLAIR (Turbo Spin Echo with inversion recovery, TR=9000, TE=105 ms, 7 echoes/TR, inversion time=2375 ms) and T1-weighted after gadolinium contrast agent (same parameters as in the T1-weighted sequence).

We show an example of a tumor in a T2 MR image in Fig. 5(A). In this image, the tumor is located in the right center. Fig. 5(B) shows the corresponding FD image. In Fig. 5(B), each subimage represents a gray scale corresponding to its FD value. For this image, the tumor has a relatively low FD and is thus indicated primarily by darker subimages, with the exception of the upper right corner of the tumor. We obtained Fig. 5(C) and (D) assuming that the brain is symmetrical along the septum and that the tumor is located in one half of the brain. In Fig. 5(C) and (D), the results are shown as half of an image that uses the difference between the FD of each subimage on the right side of the brain and its corresponding mirrored subimage on the left side.

Algorithm 3

---

for *each sub-image*

    Define p(i,j) = gray value at (i,j)

    $u_0(i, j) = p(i, j)$

    for *r = 1 to 6*

$$u_r(i, j) = \max \left\{ u_{r-1}(i, j) + 1, \max_{|(k,l)-(i,j)| \leq 1} u_{r-1}(k,l) \right\}$$

    Compute blanket volume:

$$V_r = \sum_{(i,j)} [u_r(i, j) - p(i, j)]$$

    Compute blanket surface area: $A_r = V_r - V_{r-1}$

    To compute fractal dimension (D):

    $log(A_r) = (2 - D)*log(r) + K'$

    FD = slope of log(A_r) vs. log(r)

Fig. 4. Pseudocode for the blanket algorithm [15].

Table 1
Image data set by source and modality

Source	T1 without contrast	T1 with contrast	T2 without contrast	T2 with contrast	FLAIR	Proton density without contrast	CT without contrast	CT with contrast
ACR	3	2	11	3	0	4	8	4
SJ	7	7	7	15	7	2	0	0

Specifically, Fig. 5(C) shows an example of an FD image containing only subimages wherein the FD is lower on the tumor (right) side. Conversely, Fig. 5(D) shows an example of an FD image containing only subimages for which the subimage FD is higher on the tumor side. We denote these two cases as negative FD difference and positive FD difference, respectively, for the remainder of the discussion. Furthermore, we use brighter pixels to represent a larger FD difference between the halves of the image in the specified negative or positive direction. Since most of the tumor has a lower FD in Fig. 5(B), tumor location is identified by the brightest subimages in the negative FD difference image in Fig. 5(C). However, the upper right corner of the tumor has a higher FD in Fig. 5(B) and is thus identified by the brightest subimage in Fig. 5(D).

After we computed the FD, the statistical efficacy of each algorithm for tumor detection was determined. The efficacy was determined by comparing the FD results with the actual tumor location. Fig. 6(A) shows an example of a T2 MR brain tumor image. The actual tumor location was determined from a manually segmented image, as shown in Fig. 6(B), wherein the white pixels indicate the tumor volume. A subimage was excluded from the statistical analyses if more than one third of its pixels fell outside the brain tissue area. Thus, in Fig. 5(C) and (D), the peripheral subimages are not displayed. By excluding these subimages, we minimized the interference in tumor detection resulting from variations in the background of the image outside the brain area. Finally, we computed the statistical efficacy of our FD tumor detection algorithms as follows:

(1) FD of tumor area vs. that of nontumor area: The average FD of the tumor area was computed using a weighted average method. For this weighted average method, a subimage containing only 40%

tumor pixels was given 40% of the weight of a subimage containing 100% tumor pixels. The average nontumor FD was computed using the same method. The mean and standard deviation (s_x) of the tumor and nontumor FD were computed from all the images in this study. Next, we used the one-factor analysis of variance (ANOVA) statistical test to test for a significant difference between the mean FD of tumor area and that of the nontumor area. We used a probability level <.05 or <.01 to denote whether there is a statistical difference between tumor and nontumor regions.

(2) FD of tumor half vs. that of nontumor half: The one-factor ANOVA statistical test was used to test for a significant difference between the mean FD of the half of the brain containing the tumor and the mean FD of the other half, with $P<.05$ or $P<.01$.

(3) Negative FD difference between tumor and nontumor subimages: First, we obtained the FD difference between each subimage in the tumor half of the image and its corresponding subimage in the nontumor half. Then, all of the positive differences (wherein the FD of the subimage in the tumor half is greater than that of the subimage in the other half) were ignored. Finally, the one-factor ANOVA statistical test was used to test for a significant difference ($P<.05$ or $P<.01$) between the remaining FD differences in the tumor area and those in the nontumor area. As in Step (1), the weighted average method was used for subimages that partially contained the tumor area. For images such as that in Fig. 5(C), the ANOVA test indicated the accuracy of each subimage with a lower FD in locating the tumor.
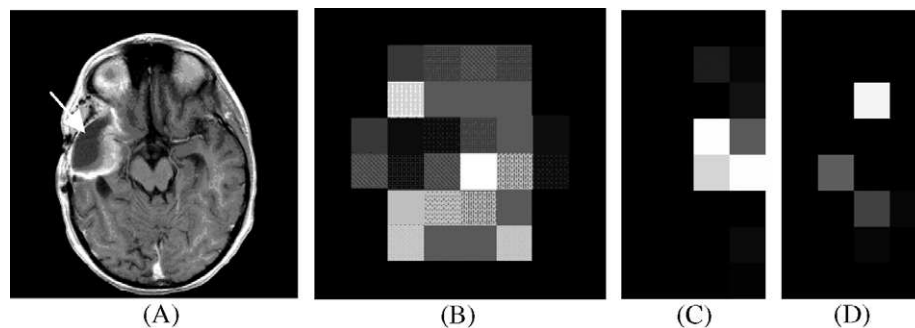

Fig. 5. (A) T2 MR image. (B) FD results for the whole MR image with an 8×8 FD subimage matrix. (C) 8×4 negative FD difference matrix for the right-half MR image. (D) 8×4 positive FD difference matrix for the right-half MR image.
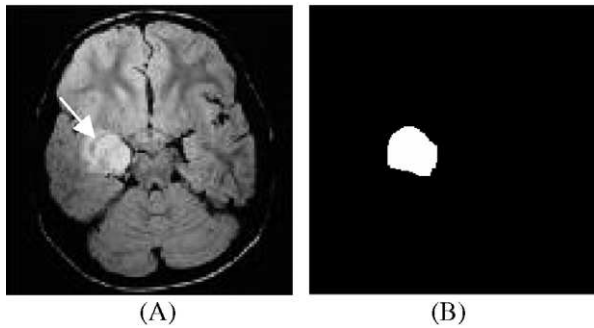
Fig. 6. (A) T2 MR image. (B) Image with manually segmented tumor.

(4) Positive FD difference between tumor and non-tumor subimages: First, we obtained the FD difference between each subimage in the tumor half of the image and its corresponding subimage in the nontumor half. Then, all of the negative differences (wherein the FD of the subimage in the tumor half is less than that of the subimage in the nontumor half) were ignored. Finally, the one-factor ANOVA statistical test was used to test for a significant difference ($P<.05$ or $P<.01$) between the remaining FD differences in the tumor area and those in the nontumor area. As in Steps (1) and (3), the weighted average method was used for sub-images that partially contained the tumor area. For images such as that in Fig. 5(D), the ANOVA test indicated the accuracy of each subimage with a higher FD in locating the tumor.

4. Results and discussion

We first examine selected results from specific images to demonstrate the qualitative efficacy of the fractal algorithms. To facilitate the references to different algorithms and resolutions, the following notations are used: *Blnkt8/16* to indicate that the results are obtained using the blanket algorithm by dividing each test image into 8×8 or 16×16 subimages and, similarly, *PMBC32A* to indicate that the results are obtained using the PMBC algorithm with 32×32 subimages and then taking the average of the FD for nontranslated and translated subimages.

4.1. Image-specific results

We show an example of a T1 MR (with contrast agent) image from SJ in Fig. 7(A). In Fig. 7(A), the tumor has a high FD due to the relatively rough surface of the tumor. Consequently, PMBC32A detects the tumor as high FD while PMBC64A detects tumor edges as high FD, as shown in Fig. 7(B) and (C), respectively. For the same image, PTPSA64A detects the tumor as slightly higher FD and Blnkt64A detects part of the tumor as higher FD, as shown in Fig. 7(D) and (E), respectively. By averaging the translated and nontranslated results, the effect of translation variance may be minimized. However, the averaging operation also smoothes out some high-frequency features. For the same MR image, shown again in Fig. 8(A), the tumor again exhibits a high FD for Blnkt32 and Blnkt64, as shown in Fig. 8(D) and (E), respectively. Furthermore, we noticed a lower FD around the area surrounding the tumor for Blnkt8 and Blnkt16, as shown in Fig. 8(B) and (C), respectively. This lower FD may be due to edema surrounding the tumor.

In the T1 MR (with no contrast agent) image from ACR in Fig. 9(A), the tumor contains more uniform gray values. Consequently, we obtained a low FD for the tumor with Blnkt8/16/32. However, due to the higher resolution, Blnkt64 offers a low FD in the center of the tumor and a high FD around the edges, as shown in Fig. 9(E). A higher FD exists around the edges of the tumor due to the texture of the transition from tumor to nontumor pixels.

Note that for the above examples, the results vary depending on the modality of the image, the type of tumor, the algorithm and the resolution of the subimages. For example, in the T1 MR (with contrast agent) images in Figs. 7 and 8, the PMBC32A and PTPSA64A algorithms show the tumor as a low FD while the PMBC64 algorithm shows only the tumor edges as a low FD. For the same image, the Blnkt8 algorithm detects the tumor as a high FD while the surrounding edema has a low FD. In addition, for the T1 MR (with no contrast agent) image in Fig. 9, Blnkt8/16/32 detect the tumor as a low FD while Blnkt64 detects the tumor as a high FD. Thus, to quantitatively qualify the findings, we performed statistical analysis of our results. The statistical results are obtained separately for each of the two image sets using the four statistical methods listed in Image
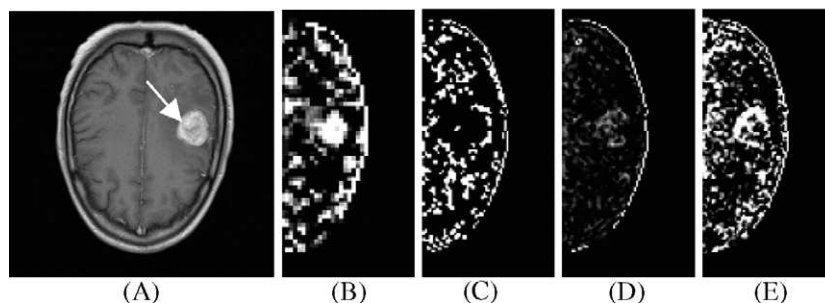

Fig. 7. (A) T1 MR image with contrast agent. Also shown are positive FD difference results for (B) PMBC32A, (C) PMBC64, (D) PTPSA64A and (E) Blnkt64A.
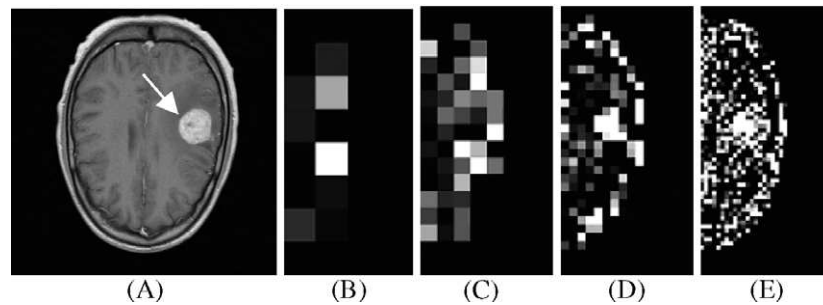
Fig. 8. (A) T1 MR image with contrast agent. Also shown are negative FD difference results for (B) Blnkt8 and (C) Blnkt16 and positive FD difference results for (D) Blnkt32 and (E) Blnkt64.

Data Set and Methods. We present a summary of our statistical analysis below.

4.2. Statistical analysis

(1) FD of tumor area vs. that of nontumor area: The statistical results for the average FD of the tumor area in comparison with the average FD of the nontumor area are shown in Table 2. Columns 3 and 4 of Table 2 show the sample mean± 1 s_x for the average tumor FD and nontumor FD, respectively. Statistical significance of the difference was computed with the one-factor ANOVA method, with P values shown in column 5. The average FD of the tumor area was lower than that of the nontumor area for all algorithms. There was a significant difference with 99% certainty for Blnkt16/32/64 and PTPSA8/16. The most significant difference was obtained by the PTPSA8 algorithm, suggesting that PTPSA8 is the most effective algorithm in delineating tumor from nontumor tissue. When analyzing the images in two separate groups by origin (ACR and SJ), the results are not significantly different for most of the algorithms. However, the PMBC32 algorithm shows that the tumor FD is significantly higher for ACR images while the tumor FD is significantly lower for SJ images. Note also that for all algorithms at higher resolutions, the mean FD is greater than 3.0, which should never be true for 2D fractal surfaces. This anomaly in FD may be due to

the loss of fractal characteristics in the digital image when the subimages become too small at higher resolutions. However, the higher resolutions often show a meaningful FD difference between tumor and nontumor areas, as shown in Table 2. The relatively high s_x of the FD values prevents any single algorithm from being used exclusively to identify the tumor area. However, since many of the algorithms statistically indicate possible tumor areas, these algorithms may be combined for successful tumor segmentation.

(2) FD of tumor half vs. that of nontumor half: Table 3 shows the one-factor ANOVA statistical analysis of the FD difference between the tumor and nontumor halves. Column 3 in Table 3 presents a comparison of the average FD for the tumor half with that of the nontumor half. The PTPSA8 algorithm is the only one for which there is a statistically significant difference, with $P<.01$. These findings on the PTPSA algorithms for the half image are consistent with the above results for the whole-image analysis. Thus, the PTPSA8 algorithm may be used to ascertain which half of the image contains the tumor.

(3) Negative FD difference of tumor vs. nontumor subimages: As discussed above for the whole-image results, the FD of tumor regions is significantly lower than the FD of the nontumor regions for most cases in Table 2. Consequently, we may expect that when comparing subimages between the halves of the image, a negative difference may
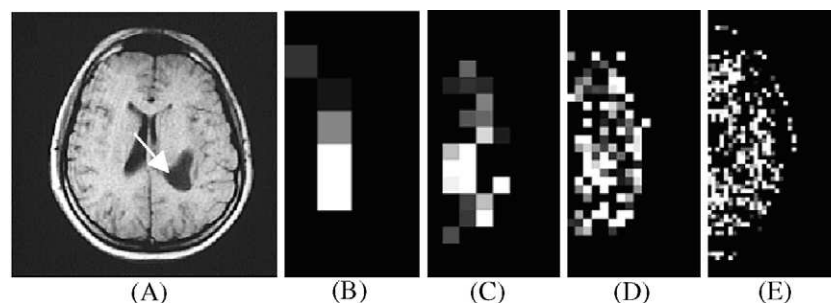

Fig. 9. (A) T1 MR image without contrast agent. Also shown are negative FD difference results for (B) Blnkt8, (C) Blnkt16 and (D) Blnkt32 and positive FD difference results for (E) Blnkt64.

Table 2
Comparison of average tumor FD with that of nontumor FD in a set of 80 images

Algorithm	Resolution	Average tumor FD (mean$\pm s_x$)	Average nontumor FD (mean$\pm s_x$)	Significant difference
PMBC	8×8	2.522±0.118	2.535±0.097	None
	16×16	3.078±0.153	3.113±0.095	$P<.05$
	32×32	3.172±0.162	3.174±0.110	None
	64×64	2.106±0.112	2.133±0.065	$P<.05$
PTPSA	8×8	2.668±0.166	2.788±0.077	$P<.01$
	16×16	3.175±0.231	3.239±0.073	$P<.01$
	32×32	3.318±0.276	3.327±0.109	None
	64×64	3.988±0.152	4.024±0.093	$P<.05$
Blanket	8×8	2.561±0.174	2.597±0.163	None
	16×16	2.626±0.182	2.694±0.169	$P<.01$
	32×32	2.788±0.182	2.874±0.154	$P<.01$
	64×64	3.296±0.342	3.409±0.212	$P<.01$

indicate the position of the tumor. This hypothesis is confirmed by the results in column 4 of Table 3. The tumor region is best identified with the PTPSA8 and Blnkt16 algorithms, with $P<.01$. The tumor region is also indicated by the PTPSA16, Blnkt8 and Blnkt32 algorithms, with $P<.05$. As expected, these algorithms in Table 3 correspond to the algorithms in Table 2 that have the most significant differences between tumor FD and nontumor FD.

(4) Positive FD difference of tumor vs. nontumor subimages: As expected from the above discussion of whole-image results, a positive FD difference between subimages does not indicate the tumor location in most cases. This observation is confirmed by the results in column 5 of Table 3. The only case wherein a positive FD difference indicates the tumor location is the PMBC8 algorithm, with $P<.05$. Thus, it may be possible to use the PMBC8 algorithm to detect tumors that have more complex textured surfaces.

5. Conclusion and future work

In this study, we show that the FD is a statistically significant indicator for tumor identification in a set of 80 MR and CT brain images. Specifically, our statistical analyses suggest the following two conclusions about tumor location identification using FD techniques. First, tumor location is identified by subimages that have an FD lower than the average FD of the nontumor tissue. Second, tumor location is identified by a negative FD difference between a subimage in one half and its corresponding subimage in the other half of an image. The first conclusion is useful even in cases wherein the tumor spans both halves of the brain. Furthermore, the first conclusion is valid for a single brain image even when the image is not centered and aligned correctly. In contrast, the second conclusion requires the image to be aligned correctly for best comparison of the

halves of the brain. However, the second conclusion is less sensitive to the natural variations in FD within the brain since these variations may cause the first conclusion to falsely identify natural variations as tumor regions. Thus, the two methods may be combined in the future for higher sensitivity in fractal-based tumor identification.

While each algorithm often detects a specific tumor differently, it is likely that these algorithms may be used in a complementary fashion. For example, lower subimage resolutions may be used to locate the general area of the tumor before applying higher subimage resolutions to locate the tumor more precisely. Specifically, the PTPSA algorithm is more predictive at lower resolutions and the blanket algorithm is more predictive at higher resolutions. Furthermore, the PTPSA8 algorithm offers the best tumor detection performance, as evidenced from the above statistical analyses.

In this study, note that the FD of tumor regions is generally lower than that of the nontumor regions. Since the FD is indicative of the roughness of the 3D density surfaces [12,15,18], tumors in brain MR or CT images are generally expected to offer either higher or lower FD values when compared with the surrounding healthy tissues. The higher or lower FD values are thus indicative of the higher or lower roughness of the tumor surface in MR or CT images. However, the higher or lower FD values in MR or CT images may depend on various factors including the type of tumor imaged and the contrast agent used in the study. For example, in MR images, malignant gliomas are characterized by (a) ragged boundaries; (b) initially only in white matter, possibly later spreading outside white matter; (c) only margins enhance with contrast agent; and (d) accompanied by edema [19]. In contrast, meningiomas are characterized by (a) smooth boundaries; (b) usually occupying space; and (c) smoothly and fully enhancing with contrast [19]. In our current study, the primary goal is to identify the efficacy of FD analysis in delineating the differences between tumor and nontumor tissue only. Future work may include analysis of FD of known tumor types using known contrast agents in MR and CT images.

Table 3
Results from comparing the FD of the subimages in the tumor half with that of the nontumor half

Algorithm	Resolution	Tumor half difference	Negative FD difference	Positive FD difference
PMBC	8×8	None	None	$P<.05$
	16×16	None	None	None
	32×32	None	None	None
	64×64	None	None	None
PTPSA	8×8	$P<.01$	$P<.01$	None
	16×16	None	$P<.05$	None
	32×32	None	None	None
	64×64	None	None	None
Blanket	8×8	None	$P<.05$	None
	16×16	None	$P<.01$	None
	32×32	None	$P<.05$	None
	64×64	None	None	None

Further future work may include examining the effects of tumor type and size as well as the effect of noise in FD analysis. Different methods of combining translated and nontranslated results may also be examined in the future. Furthermore, results from multiple image frames in the same patient brain may be combined to obtain the 3D volume of a tumor. Finally, image fusion may be used to combine different imaging modalities, algorithms and resolutions to increase the sensitivity and specificity of the FD analysis for use in clinical settings.

Acknowledgments

References

[1] Gering D, Nabavi A, Kikinis R, Hata N, Odonnell L, Eric W, et al. An integrated visualization system for surgical planning and guidance using image fusion and an open MR. Magn Reson Imaging 2001;13:967–75.

[2] Joe BN, Fukui MB, Meltzer CC, Huang Q, Day RS, Greer PJ, et al. Brain tumor volume measurement: comparison of manual and semiautomated methods. Radiology 1999;212:811–6.

[3] Gibbs P, Buckley DL, Blackband SJ, Horsman A. Tumour volume determination from MR images by morphological segmentation. Phys Med Biol 1996;41:2437–46.

[4] Serra J. Image analysis and mathematical morphology. London: Academic Press; 1982.

[5] Zhu Y, Yan H. Computerized tumor boundary detection using a Hopfield neural network. IEEE Trans Med Imaging 1997;16:55–67.

[6] Collins DL, Peters TM, Dai W, Evans AC. Model based segmentation of individual brain structures from MRI data. SPIE Proceedings of the 1st International Conference on Visualization in Biomedical Computing 1992;1808:10–23.

[7] Clarke LP, Velthuizen RP, Camacho MA, Heine JJ, Vaidyanathan M, Hall LO, et al. MRI segmentation: methods and applications. Magn Reson Imaging 1995;13:343–68.

[8] Gerig G, Martin J, Kikinis R, Kübler O, Shenton M, Jolesz FA. Unsupervised tissue type segmentation of 3D dual-echo MR head data. Image Vis Comput 1992;10:349–60.

[9] Vannier MW, Butterfield RL, Rickman DL, Jordan DM, Murphy WA, Biondetti PR. Multispectral magnetic resonance image analysis. Radiology 1985;154:221–4.

[10] Falcao AX, Udupa JK, Samarasekera S, Sharma S. User-steered image segmentation paradigms: live wire and live lane. Graph Models Image Process 1998;60:233–60.

[11] McInnerney T, Terzopoulos D. Deformable models in medical image analysis: a survey. Med Image Anal 1996;1:91–108.

[12] Iftekharuddin KM, Jia W, Marsh R. A fractal analysis of tumor in brain MR images. Mach Vis Appl 2003;13:352–62.

[13] Sarkar N, Chaudhuri BB. An efficient approach to estimate fractal dimension of textural images. Pattern Recogn 1992;23:1035–41.

[14] Clarke KC. Computation of the fractal dimension of topographic surfaces using the triangular-prism-surface-area method. Comput Geosci 1986;12:713–22.

[15] Zheng L, Chan AK. An artificial intelligent algorithm for tumor detection in screening mammogram. IEEE Trans Med Imaging 2001;20:559–67.

[16] Penn AI, Bolinger L, Schnall MD, Loew MH. Discrimination of MR images of breast masses with fractal-interpolation function models. Acad Radiol 1999;6:156–63.

[17] Kido S, Kuriyama K, Higashiyama M, Kasugai T, Kuroda C. Fractal analysis of internal and peripheral textures of small peripheral bronchogenic carcinomas in thin-section computed tomography: comparison of bronchioloalveolar cell carcinomas with nonbronchioloalveolar cell carcinomas. J Comput Assist Tomogr 2003;27:56–61.

[18] Iftekharuddin KM, Parra C. Multiresolution-fractal feature extraction and tumor detection: analytical modeling and implementation. Proc SPIE 2003;5207:801–12.

[19] Moon N, Bullitt E, van Leemput K, Gerig G. Model-based brain and tumor segmentation. In: Kasturi R, Laurendeau D, Suen C, IEEE Computer Society, editors. IEEE Proc 16th Int Conf on Pattern Recognition ICPR; 2002. p. 528–31.